# Evaluating the extent of cell death in 3D high frequency ultrasound by registration with whole-mount tumor histopathology[a)]

Roxana M. Vlad[b)]
*Radiation Medicine Program, Princess Margaret Hospital, Toronto, Ontario M5G 2M9, Canada and Department of Radiation Oncology, Faculty of Medicine, University of Toronto, Toronto, Ontario M5G 2M9, Canada*

Michael C. Kolios
*Department of Medical Biophysics, University of Toronto, Toronto, Ontario M5G 2M9, Canada and Department of Physics, Ryerson University, Toronto, Ontario M5B 2K3, Canada*

Joanne L. Moseley
*Radiation Medicine Program, Princess Margaret Hospital, Toronto, Ontario M5G 2M9, Canada*

Gregory J. Czarnota
*Department of Radiation Oncology, Faculty of Medicine, University of Toronto, Toronto, Ontario M5G 2M9, Canada; Department of Medical Biophysics, University of Toronto, Toronto, Ontario M5G 2M9, Canada; and Imaging Research, Sunnybrook Health Sciences Centre, Toronto, Ontario M4N 3M5, Canada*

Kristy K. Brock
*Radiation Medicine Program, Princess Margaret Hospital, Toronto, Ontario M5G 2M9, Canada and Department of Medical Biophysics, University of Toronto, Toronto, Ontario M5G 2M9, Canada*

(Received 3 December 2009; revised 1 June 2010; accepted for publication 11 June 2010; published 23 July 2010)

**Purpose:** High frequency ultrasound imaging, 10–30 MHz, has the capability to assess tumor response to radiotherapy in mouse tumors as early as 24 h after treatment administration. The advantage of this technique is that the image contrast is generated by changes in the physical properties of dying cells. Therefore, a subject can be imaged before and multiple times during the treatment without the requirement of injecting specialized contrast agents. This study is motivated by a need to provide metrics of comparison between the volume and localization of cell death, assessed from histology, with the volume and localization of cell death surrogate, assessed as regions with increased echogeneity from ultrasound images.

**Methods:** The mice were exposed to radiation doses of 2, 4, and 8 Gy. Ultrasound images were collected from each tumor before and 24 h after exposure to radiation using a broadband 25 MHz center frequency transducer. After radiotherapy, tumors exhibited hyperechoic regions in ultrasound images that corresponded to areas of cell death in histology. The ultrasound and histological images were rigidly registered. The tumors and regions of cell death were manually outlined on histological images. Similarly, the tumors and hyperechoic regions were outlined on the ultrasound images. Each set of contours was converted to a volumetric mesh in order to compare the volumes and the localization of cell death in histological and ultrasound images.

**Results:** A shrinkage factor of $17 \pm 2\%$ was calculated from the difference in the tumor volumes evaluated from histological and ultrasound images. This was used to correct the tumor and cell death volumes assessed from histology. After this correction, the average absolute difference between the volume of cell death assessed from ultrasound and histological images was $11 \pm 14\%$ and the volume overlap was $70 \pm 12\%$.

**Conclusions:** The method provided metrics of comparison between the volume of cell death assessed from histology and that assessed from ultrasound images. It was applied here to evaluate the capability of ultrasound imaging to assess early tumor response to radiotherapy in mouse tumors. Similarly, it can be applied in the future to evaluate the capability of ultrasound imaging to assess early tumor response to other modalities of cancer treatment. The study contributes to an understanding of the capabilities and limitation of ultrasound imaging at noninvasively detecting cell death. This provides a foundation for future developments regarding the use of ultrasound in preclinical and clinical applications to adapt treatments based on tumor response to cancer therapy.  [DOI: 10.1118/1.3459020]

Key words: ultrasound, tumor response, registration, whole-mount tumor histopathology, finite element modeling

## I. INTRODUCTION

The assessment of tumor response to treatment is an important aspect of the preclinical and clinical development and evaluation of cancer therapeutics. Tumor responses to treatment are traditionally assessed by measurements of tumor size in clinical images using the response evaluation criteria in solid tumors guidelines.[1,2] These criteria are based on the measurement of the largest diameter of a tumor, as measured from computed tomography or magnetic resonance imaging. Since tumor shrinkage can take weeks or even months to become apparent, evaluation of tumor response using these criteria is typically conducted at 6–8 weeks after treatment starts. The limitations of this approach and the necessity of considering different criteria to evaluate tumor response, earlier during the treatment, have been previously discussed.[3]

In recent years, measurements of tumor size have been supplemented by imaging of tissue function using different imaging techniques, i.e., positron emission tomography (PET), dynamic contrast-enhanced magnetic resonance imaging (DCE-MRI), magnetic resonance spectroscopy, and Doppler ultrasound using antivascular contrast agents.[4] These techniques are based on the imaging of markers of response that can predict changes in cell tumor metabolism, inhibition of cell proliferation, and cell death[4–7] with the aim of providing information about changes in tumor biology and assessing response to treatment earlier, often before there is any change in tumor size. From this category, PET imaging, using a glucose analog, the radionuclide 2-[18F] fluoro-2-deoxy-d-glucose (FDG) is an established modality in the diagnosis and management of various malignancies.[4] Since early radiotherapy effects include inflammatory reactions that can result in FDG uptakes comparable to tumor uptakes, it has been frequently recommended that FDG-PET be performed several months after completion of radiotherapy.[8] For this reason, most clinical studies using FDG-PET imaging were performed on tumors treated with chemotherapy or with new experimental therapies, and less data are available in terms of specifically assessing tumor responses to radiotherapy. In DCE-MRI, a series of rapidly acquired images are used to follow the kinetic of a contrast agent inflow into the tumor following the intravenous injection of the agent. This technique has been used clinically to assess tumor response to radiotherapy in different types of cancers including cancers of head and neck and carcinoma of the cervix, and to predict survival in breast cancer.[9–13] Despite their effectiveness, these methods, FDG-PET and DCE-MRI, are limited by their cost and the requirement of injecting a radioactive substance or a contrast agent for each assessment. Furthermore, it is not yet well known which time points, after treatment delivery, are appropriate to assess tumor response using these techniques. For these reasons, these imaging techniques have a reduced applicability in longitudinal preclinical and clinical studies and, currently, no imaging modality is used routinely in the clinic to assess tumor response within hours to days after the delivery of a treatment.

Recent publications have indicated that ultrasound imaging (10–60 MHz) and quantitative ultrasound can be used to detect cell death in tumor xenografts exposed to radiotherapy and photodynamic therapy.[14,15] In these studies, regions of tumor demonstrating increases of echogeneity in ultrasound images and changes in spectral parameters, in comparison with baseline pretreatment parameters were identified in histology as areas of cell death. It is important to note that even at these high frequencies, individual cells cannot be resolved. The ultrasound images produced have the typical speckle pattern seen in conventional ultrasound images, with an increase of the brightness of the speckle pattern in the regions that correspond to areas of cell death in histology. These regions with increases of the brightness of the speckle pattern in ultrasound images are referred as *hyperechoic regions* in this study.

The mechanisms by which high frequency ultrasound is sensitive to cell death have been documented in previously published works.[16–19] Briefly, the increases in ultrasound backscatter, identified as hyperechoic regions in ultrasound images, are related to changes in tissue scatterer properties, e.g., size, number density, relative acoustic impedance, and spatial organization. For instance, previous experimental investigations[16–19] have indicated that the contrast between the regions that responded to therapy and regions that did not can be related to a combination of nuclear changes (i.e., nuclear condensation and fragmentation) following the sequence of apoptotic cell death.

The clinical management of tumor treatment remains a significant challenge because tumors are phenotypically heterogeneous and, therefore, it is rare for all cancers of a particular type to respond to a specific therapy.[20] Traditional prognostic factors of tumor response based on the measurement of tumor size are not ideal for predicting patient outcome because these are applied late during the course of therapy. A noninvasive technique, such as high frequency ultrasound, capable of assessing early tumor responsiveness to therapy within days after the start of a treatment, could aid clinicians in making decisions to guide treatment selection, i.e., selecting a treatment based on tumor aggressiveness, and ultimately help in providing individualized patient treatment. In order to adopt high frequency ultrasound imaging to preclinical and clinical applications, it is essential to know how well the volume of cell death, assessed noninvasively from ultrasound, corresponds to the true volume of cell death assessed from histology.

Currently, stained histological sections are considered the "gold standard" for cancer diagnosis, detection of cell death, and assessment of tumor response. Whole-mount sectioning techniques have been introduced recently with the advent of extended pathological methods. Some of the applications focus on providing databases for education and research[21] and developing algorithms to improve cancer detection in different imaging techniques for an accurate estimation of cancer margins and the location of multiple foci.[22–24] Generally, whole-mount serial sections are expensive techniques, imposing stringent specifications on tissue processing protocols.

The objective of this study was to provide an understanding of the capabilities and limitations of ultrasound imaging

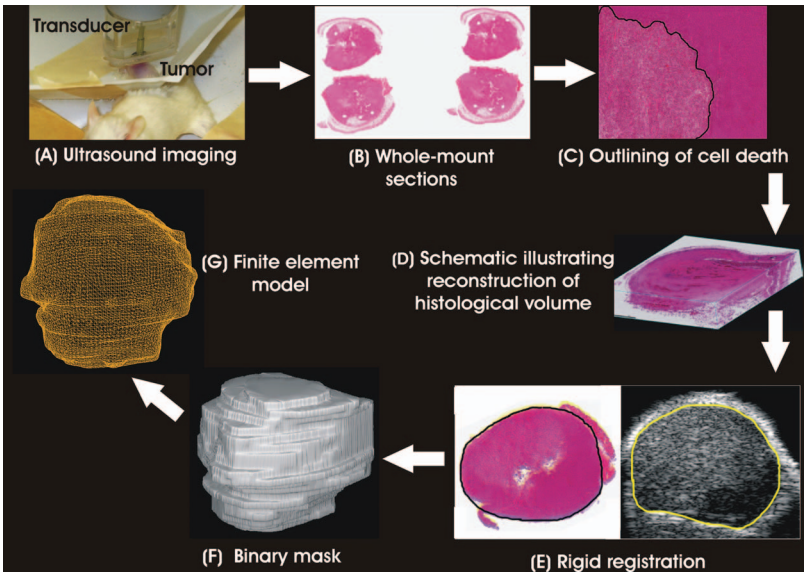


FIG. 1. Flow chart illustrating the main steps of the process: (A) Ultrasound data collection; (B) histological sections of a whole tumor mounted on a slide of $1\times3$ in.; (C) outlining of cell death on a histological section at a higher magnification of 20×; (D) reconstruction of a histological volume by aligning consecutive slides; (E) rigid registration of histological and ultrasound images and delineating a tumor on ultrasound and histological images; (F) contours conversion to a binary mask; and (G) conversion of a mask file to a finite element model.

to detect cell death noninvasively in mouse tumors. A novel method was developed to quantitatively compare the size and spatial location of the volume of cell death identified in histological images to that of cell death assessed from high frequency ultrasound images using frequencies of 12–30 MHz. It was applied here to detect early tumor response to radiotherapy, but, similarly, could be applied to assess tumor response to other modalities of cancer treatment. The method uses histopathological volume reconstruction of whole-mount tumor xenografts at 24 h after treatment with radiation and compares the geometry of cell death assessed from gold standard histology to cell death segmented as hyperechoic regions from ultrasound images.

## II. METHODS

A flow chart describing the steps involved in the process is illustrated in Fig. 1 and will be described in the following sections.

### II.A. Xenograft tumor models

This study used three mouse models of human tumors, four nasopharyngeal carcinoma tumors (grown from C666–1 cell line), three squamous cell carcinoma tumors of the pharynx (grown from FaDu cell line), and one prostatic carcinoma tumor (grown from PC3 cell line). These models were selected to exemplify different patterns of cell death following radiotherapy; C666–1 and FaDu tumors respond well to radiotherapy,[19] whereas PC3 tumor is not responsive. For instance, PC3 tumors presented just sporadic patches of apoptotic cell death[25] when treated with radiation doses from 2 to 8 Gy. This pattern has been repeatedly reported in PC3 tumors and[25,26] therefore, it was chosen in this study as an illustrative example of nonresponsive tumor. All animal experiments were conducted in accordance with the guidelines of the Animal Care Committee (Sunnybrook Health Sciences Center, Ontario, Canada) and satisfied all rules for the use of laboratory animals. In all experiments, 6–8 week-old severe combined immunodeficient (SB-17, SCID) male mice were used.

The FaDu and PC3 cell lines were obtained from the American Type Culture Collection. The C666–1 cells[27,28] were maintained in RPMI 1640 cell culture media supplemented with 10% fetal bovine serum (FBS) and antibiotics (100 mg/L penicillin and 100 mg/L streptomycin). The FaDu cells were cultured in Eagle's minimum essential media with 2 mM L-glutamine and Earle's balanced salt solution adjusted to contain 1.5 g/L sodium bicarbonate, 1.0 mM sodium pyruvate, and 10% FBS. The PC3 cells were cultured in Kaighn's modification of Ham's F12 media supplemented with streptomycin (100mg/l) and 10% FBS.

C666–1 ($\sim10^6$), PC3 ($\sim10^6$) and FaDu ($\sim10^5$) cells were injected intradermally into the left hind leg of each mouse. Primary tumors were allowed to develop for approximately 2–4 weeks until they reached a diameter of 6–10 mm.

Prior to imaging, the mice were anaesthetized and the tumors and surrounding area were depilated. Anesthesia consisted of 100 mg/kg ketamine, 5 mg/kg xylazine, and 1 mg/kg acepromazine in 0.1 ml saline injected intraperitoneally. This sedated the mice for approximately 1 h, sufficient time for the entire imaging and irradiation procedure.

### II.B. Administration of ionizing radiation

Tumors were irradiated with radiation doses of 2, 4, and 8 Gy in single fractions using a small animal irradiator (Faxitron Cabinet X-ray System, Faxitron X-ray Corporation, Wheeling, IL) that delivered 160 keV X rays at a rate of 200

cGy/minute. The animal was shielded using a 3 mm thick lead sheet and only the tumor was exposed through a circular cutout.

### II.C. Ultrasound data acquisition

All images were acquired with a Vevo 770 (VisualSonics Inc., Toronto, Ontario, Canada) high frequency ultrasound system. A 25 MHz single element focused transducer with a −6 dB bandwidth of 12–30 MHz, 12.5 mm focal distance, and 6 mm aperture was employed. Three-dimensional images were collected by automatically translating the transducer in the elevation dimension and acquiring 2D images every 100 $\mu$m over the maximum dimension of the tumor (~10 mm). The 2D images had a $10\times10$ mm$^2$ field of view with the tumor centered at the transducer focus. The experimental setup is shown in Fig. 1(A).

The PC3 tumor exhibited small hyperechoic regions after 8 Gy of radiation (approximately 10% of the whole tumor area). Since any minor misalignment could compromise the reconstruction of cell death volume, an extra step was introduced for this tumor. This consisted of excising the tumor, implanting three needles to create fiducial markers, and imaging the tumor *ex vivo* in the same orientation as *in vivo*. This procedure was not used for FaDu and C666–1 tumors that presented large areas of cell death because the needles can damage these areas, causing a bias in the evaluation of cell death. It is important mentioning that an accurate histopathological reconstruction and correlation of histology with imaging present serious challenges due to tissue deformation during histopathological processing, and finding appropriate markers visible on both data sets, consecutive histological slides, as well as ultrasound images. An ongoing work seeks to develop modalities of using fiducial markers to assist and test for accuracy in 3D histopathological reconstruction and registration with different imaging modalities.[29]

### II.D. Whole-mount section preparation and 3D volume reconstruction

Twenty-four hours after irradiation and immediately after final ultrasound imaging, tumors were excised, fixed in 10% neutral-buffered formalin, and then processed and embedded in paraffin. Tumors were serially sliced in the same orientation to best match the ultrasound scanning planes with a distance between sections of 0.2 mm for PC3 tumor and 0.5 mm for the rest of the tumors. Tissue slices were processed as whole-mount sections on $1\times3$ in. glass slides [Fig. 1(B)]. To detect cell death, hematoxylin and eosin (H&E) staining was performed on all tumor sections and terminal uridine deoxynucleotidyl transferase 2′-deoxyuridine 5′-triphosphate nick end labeling (TUNEL) staining was performed on selective sections collected from each tumor. H&E stain consisted in the application of the basic dye hematoxylin, which colors the nucleus and structures containing nucleic acid (e.g., nuclear fragments resulting from apoptotic cell death) with a blue-purple hue, and alcohol-based acidic eosin, which colors intracellular and extracellular protein in bright pink. TUNEL staining is a common method to detect cell death demonstrating high specificity for cells that die by apoptosis. The areas of cell death, typically, appear as brown-colored regions in histological sections stained using TUNEL technique.

Histological sections were digitized as whole slides at a magnification of 20× and high resolution of 0.5 $\mu$m/pixel using a TISSUEscope™ 4000 (Biomedical Photometrics Inc., Waterloo, Ontario, Canada). The images were stored in a digital file enabling low-resolution and high-resolution views of whole tumor slices [Figs. 1(B) and 1(C)]. The areas of cell death were strictly defined as tumor regions presenting typical characteristics of cell death by apoptosis, specifically nuclear fragmentation and condensation. The largest area of cell death was outlined on each high-resolution view of the tumor, and then the entire section was captured at a low resolution using Aperio's (Aperio Technologies, Vista, CA) image viewer, ImageScope. Since tumors could have small regions of spontaneous cell death without exposure to therapy, we considered that small isolated patches of cell death were not representative for tumor response to radiotherapy. An in-house developed algorithm (Mathworks Inc., Natick, MA) consisting of two rigid translation and one rotation was used to manually align anatomical landmarks, e.g., bundles of muscles, skin, and marks created by the implanted needles (where they existed) on serial histological sections. The whole tumor volume was reconstructed as a stack of images and stored at a $0.0085\times0.0085\times z$ mm$^3$ voxel size, where $z$ represents the distance between serial sections [Fig. 1(C)].

### II.E. Data analysis

Each set of 2D images, from ultrasound and histology, was imported into a radiotherapy treatment planning system (TPS) (Pinnacle v8, Philips Medical Systems, Madison, WI) where histological images were manually registered to ultrasound images using two rigid translation and rotation [Fig. 1(E)]. Anatomical landmarks, e.g., skin and bundles of muscles, were used to guide registration of histological images to ultrasound in the TPS. After 2D registration, each set of images, histology and ultrasound, retained a single set of coordinates of the primary image (in this case of the ultrasound image). Therefore, there was no need of a subsequent 3D volume registration between the two data sets. The tumor was contoured on the ultrasound and histological images. The hyperechoic regions were also contoured on the ultrasound images. These contours produced a list of vertices, associated with each of the transverse image slices. Each separate list of vertices that resulted from outlining the tumors and regions of cell death in ultrasound and histological images, respectively, was converted from contours to a volumetric binary mask, and then exported from the TPS as a file [Figs. 1(E) and 1(F)].

The binary mask files were imported into a mathematical development environment used commonly for data visualization and analysis (Interactive Data Language, Research System Inc., Boulder, CT). An in-house developed algorithm was used to calculate the mask volumes and the overlap of

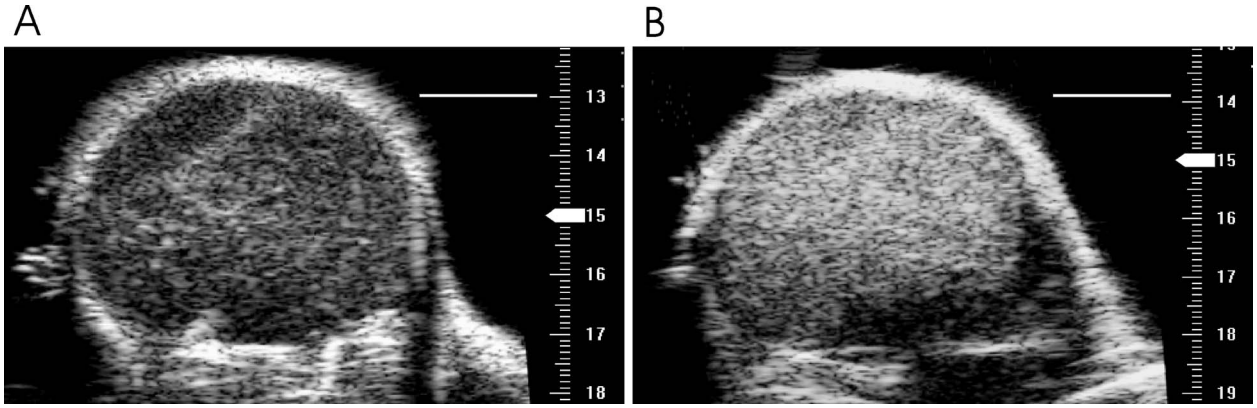


FIG. 2. Representative ultrasound images of a mouse tumor before and 24 h after radiotherapy presenting regions with increased echogeneity after radiotherapy. The white arrow on the lateral side of each tumor represents the location of the transducer focal point. Scale bars are 2 mm.

mask volumes for each representation of tumor and cell death in ultrasound and histology. The code searches data on a voxel-by-voxel basis and calculates the coordinates of each voxel in the mask file. Finally, to visualize the volumes and create models of tumor and cell death in each representation (ultrasound and histology), the mask files were converted to a triangular surface mesh using methodology described by Brock *et al.*[30] [Fig. 1(G)].

## III. RESULTS

### III.A. Qualitative assessment

The C666–1 and FaDu tumors exhibited large hyperechoic regions in ultrasound images, at 24 h after exposure to radiation, in comparison with base line parameters. Elsewhere, it has been reported[18] that the ultrasound backscatter intensity increased by 6.5–8.2 dB for the C666–1 and FaDu

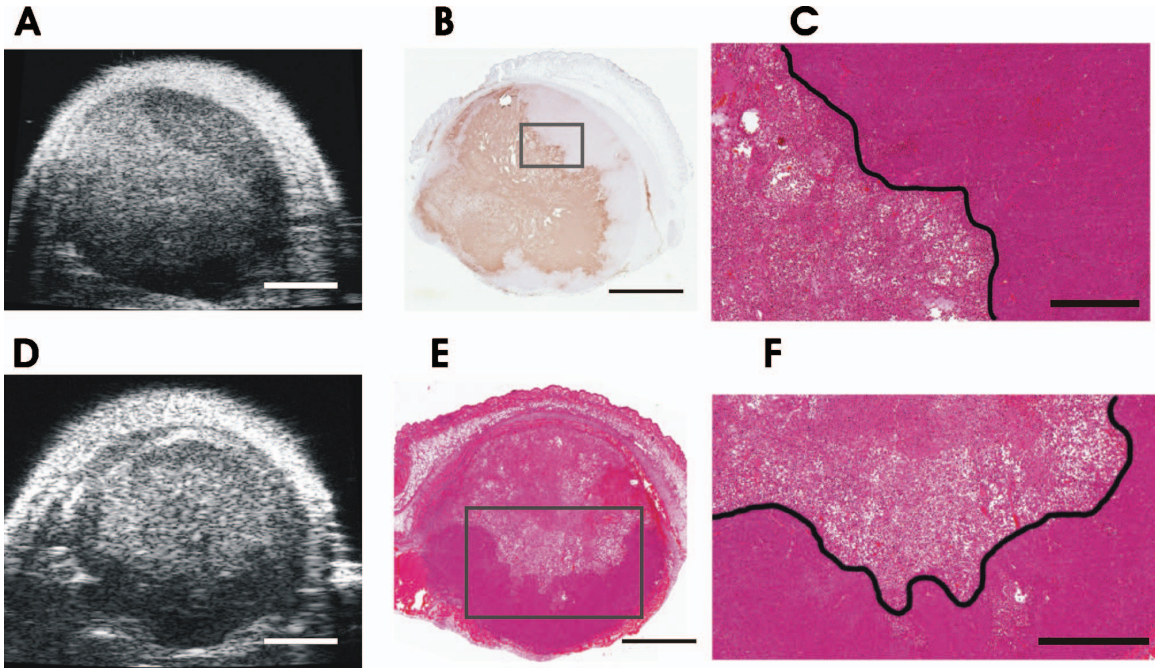


FIG. 3. Representation of cell death in high frequency ultrasound and histological images: (A) Ultrasound image of a C666–1 tumor xenograft at 24 h after treatment with 4 Gy; (B) corresponding TUNEL stained image indicating an area of cell death, the brown-colored area that has a similar shape as the hyperechoic area in the ultrasound image; and (C) higher magnification of a H&E stained image corresponding to the selection from image (B). The left side of the image (C) demarcated by the black line demonstrates the characteristics of cell death. (D) Ultrasound image of a FaDu tumor xenograft at 24 h after treatment with 8 Gy; (B) corresponding H&E stained image indicating an area of cell death of similar shape as the hyperechoic area in the ultrasound image; and (F) higher magnification of the H&E stained image corresponding to the selection from image (E), demonstrating cell death in the upper part of the image demarcated by the black line. Scale bars are 2 mm in images (A), (B), (D), and (E), 400 $\mu$m in image (C), and 1000 $\mu$m in image (F).

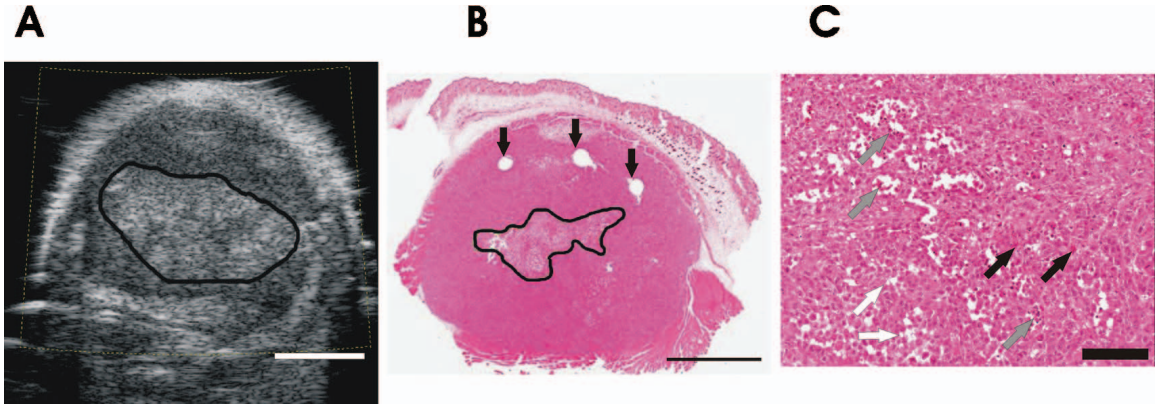


FIG. 4. (A) Ultrasound image of a PC3 tumor xenograft at 24 h after treatment with 8 Gy indicating a hyperechoic area in the middle of the tumor; (B) corresponding H&E stained image indicating an area of cell death of similar location as the hyperechoic area from the ultrasound image; the arrows indicate the marks created by the needles that helped in the alignment of histological slices for this tumor; and (C) different types of cell structural damage in PC3 tumor at 24 h after radiotherapy: The white arrow indicates microscopic edema, the black arrow indicates possible red blood cells escaping from intravascular space, and the gray arrow indicates apoptosis of endothelial cells lining blood microvasculature. Scale bars are 2 mm in images (A) and (B) and 120 $\mu$m in image (C).

tumors in these regions compared to preirradiated tumors. Representative ultrasound images of a C666–1 tumor before and 24 h after irradiation are displayed in Fig. 2. These hyperechoic regions corresponded to the areas of cell death in histological images [Fig. 3(B)]. The areas of cell death appeared as brown-colored regions in the TUNEL stained slides [Figs. 3(A) and 3(B)] and presented an appearance of discoloration of the pink eosin staining in the H&E images at low magnification [Fig. 3(E)]. This discoloration typically results because cells lose part of their protein component following cell death. At higher magnification, H&E stained images revealed a clear delineation between the regions appearing as viable tissue and areas of cell death [Figs. 3(C) and 3(F)]. The latter were characterized by smaller condensed and fragmented nuclei characteristics of apoptotic cell death.

The PC3 tumor is an example of tumor that does not respond to radiotherapy.[25,26] At 24 h after radiotherapy (8 Gy), the ultrasound image of the PC3 tumor exhibited small hyperechoic regions in the central part that appeared to correspond to areas of cell death in histology [Figs. 4(A) and 4(B)]. Some regions in the PC3 tumor revealed tissue damage observed as white microscopic spaces with little or no evidence of the characteristics of cell death by apoptosis [Fig. 4(C)]. A common explanation could be that these are histological artifacts, e.g., tissue retraction in the areas of tissue damage. However, the appearance of some red blood cells escaping from intravascular space and apoptosis of endothelial cells lining the blood vessels suggested that the tissue damage observed in these regions arise as a consequence of vascular injury. This type of cell death in hypervascular regions of a tumor can result from vascular collapse following large doses of radiation. The effect has been demonstrated by Garcia-Barros *et al.*[31] and now is supported by our recent work on PC3 tumors.[26]

### III.B. Quantitative assessment

Tumor and cell death volumes as segmented from ultrasound and histological images were presented in Table I for each tumor. There were differences between the volume of tumor assessed from ultrasound and histological images, respectively. These differences can be attributed to tissue shrinkage during histopathological processing and deforma-

TABLE I. Tumor and cell death volumes as assessed from ultrasound and histological images. The numbers in brackets from the first column represent the radiotherapy doses.

| Mouse identification | Tumor histological volume ($mm^3$) | Tumor ultrasound volume ($mm^3$) | Cell death histological volume ($mm^3$) | Cell death ultrasound volume ($mm^3$) |
|---|---|---|---|---|
| M1FaDu (2Gy) | 126 | 157 | 62 | 67 |
| M2FaDu (4Gy) | 124 | 149 | 32 | 36 |
| M3FaDu (8Gy) | 117 | 134 | 50 | 61 |
| M4C666–1 (4Gy) | 108 | 133 | 46 | 57 |
| M5C666–1 (4Gy) | 139 | 173 | 55 | 70 |
| M6C666–1 (8Gy) | 91 | 107 | 33 | 34 |
| M7C666–1 (8Gy) | 134 | 160 | 53 | 60 |
| M8PC3 (8Gy) | 193 | 231 | 11 | 22 |

tion of tissue dimensions by cutting and mounting of each section. In order to calculate a factor that accounts for these, it was considered that the 3D ultrasound volume acquired from *in vivo* tumors in live animals was the ground truth for the size of the tumor. Tumor xenografts are typically quite homogeneous in composition containing mostly cancerous cells, blood, and lymphatic vessels with no large volumes of fibrous tissue or deposits of fat. Consequently, all eight tumors (FaDu, C666–1, and PC3) were considered soft tissue of approximately similar composition and an average volumetric shrinkage factor of $17 \pm 2\%$ was calculated from all tumors. Considering that several reports[32–34] have indicated that the tissue shrinkage caused by formalin fixation does not change much between different directions and deformation of tissue resulting from cutting and mounting is small, an isometric correction was applied to all tumors in this study. Therefore, the volumes of tumor and cell death assessed from histology were scaled uniformly by 17% to account for tissue shrinkage during histopathological processing and other factors pertaining to the technique, i.e., changes in tissue by paraffin embedding, type of fixative, and time of fixation.

The differences in the volumes of tumor and cell death assessed from ultrasound and histology, before and after shrinkage correction, were plotted in Fig. 5(A). After compensating for tissue shrinkage, the average difference in the volume of tumors in ultrasound and histology decreased from $17 \pm 2\%$ to $3 \pm 2\%$. After compensating for tissue shrinkage, the average differences in the volume of cell death in ultrasound and histology decreased from $18 \pm 15\%$ to $11 \pm 14\%$ (including the PC3 tumor) and from $13 \pm 7\%$ to $6 \pm 4\%$ (excluding the PC3 tumor).

The difference in the representation of cell death in ultrasound versus histology is large (44%) for PC3 tumor versus an average of $6 \pm 4\%$ for head and neck tumors. This resulted from some sections in ultrasound images (approximately nine) that exhibited small hyperechoic regions, corresponding in histology to areas of tissue damage, but no clear appearance of cell death [Fig. 4(C)]. These regions were not considered in the calculation of the histological volume of cell death because they did not present the recognizable characteristics of apoptosis. Instead, these exhibited either a mixed phenotype (i.e., isolated clusters of cell death interspersed with clusters of cells with a normal appearance) or other types of tissue damage [Fig. 4(C)].

The volume overlap between the representation of tumor and tumor cell death in ultrasound and histological images, respectively, was plotted in Fig. 5(B). Assuming that tumor representation in ultrasound images was the ground truth, the percent of volume overlap should be 100% for a perfect identification of tumor in both modalities and perfect histological volume reconstruction and registration. The overlap of the tumor volumes as delineated from histological and ultrasound images ranged from 75% to 97%, resulting in an average overlap of $89 \pm 8\%$. The overlap of the volumes of cell death assessed from ultrasound and histological images ranged from 46% to 81% with an average of $70 \pm 12\%$.

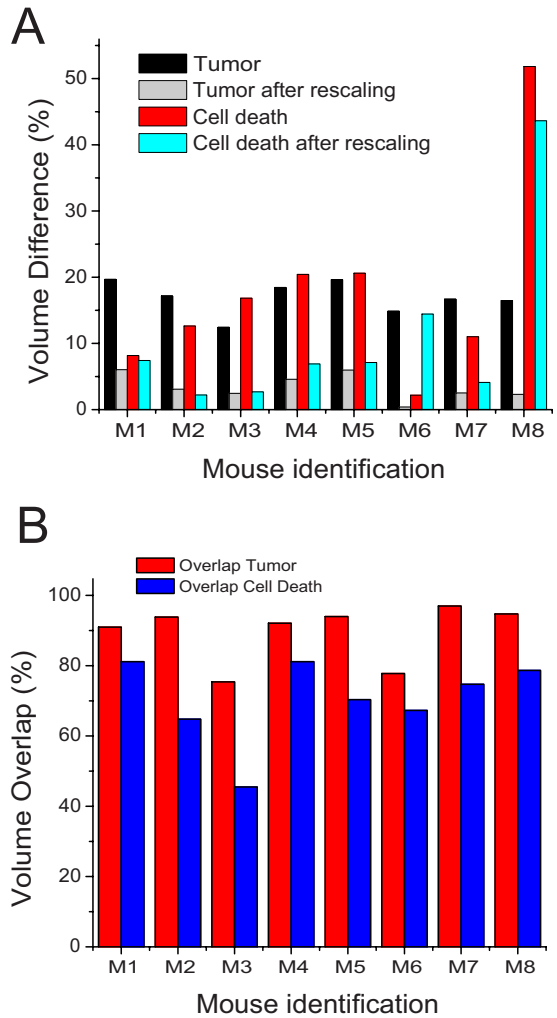


FIG. 5. Volume differences and volume overlaps of tumor and cell death in ultrasound and histology. (A) Percent differences in the volume of tumor and cell death in ultrasound and histology, before and after correction for tissue shrinkage. (B) Overlap of tumor and cell death. Volumes are relative to the volume of tumor and cell death evaluated from ultrasound images.

Finite element models of tumor and cell death representation in ultrasound and histological images with corresponding cross section for each representation were shown in Figs. 6(A)–6(D). The models indicated a good colocalization of cell death volume in the ultrasound and histological representation. Representative examples of a good overlap corresponding to mouse [M1 in Fig. 5](B) and weak overlap corresponding to mouse [M3 in Fig. 5(B)] are shown in Figs. 6(E) and 6(F).

## IV. DISCUSSION

A whole-mount pathology method for 3D tissue reconstruction and registration with high frequency ultrasound images has been developed to compare the volume of cell death evaluated from histology to the volume of hyperechoic regions identified in ultrasound images. Previous publications[14,15] used qualitative visual comparisons of histological and ultrasound images to indicate that regions of tumor presenting increases of echogeneity in ultrasound images, after

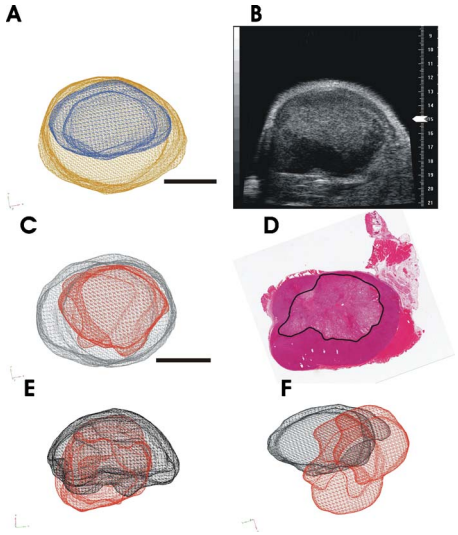


FIG. 6. (A) Finite element model of a tumor and cell death segmented from ultrasound images with (B) corresponding cross-section ultrasound image illustrating tumor orientation and the position of the transducer focal point (the white arrow on the lateral side of the ultrasound image) during scanning; (C) finite element model of tumor and cell death segmented from histology with (D) corresponding histological cross section, demonstrating an area of cell death outlined in black; finite element models illustrating the overlap of cell death derived from ultrasound and histological images, respectively, demonstrating (E) a good overlap (81%) and (F) a weak overlap (45%). Scale bars are 2 mm for all images.

anticancer therapy, corresponded to regions of cell death in histology. The method presented in this study provides metrics of comparison between the volume and localization of cell death, assessed from histology, with the volume and localization of cell death surrogate derived as hyperechoic regions from ultrasound imaging. This is important in order to evaluate the capability of high frequency ultrasound imaging to assess tumor response to therapy.

The volumetric overlap between the regions of cell death surrogate identified in ultrasound as hyperechoic regions and those delineated in histology, could be affected by different factors that can be divided into three main categories. The first category addresses factors linked to the imaging capabilities of the ultrasound machine, specifically the ultrasound transducer that defines the quality of the image (i.e., central frequency, bandwidth, focal distance, and depth of field). The effect of these factors and other factors, i.e., interobserver and intraobserver variability and mouse breathing motion, on the measurement of tumor volume has been discussed in a recent publication[35] that used a similar system as in this study. For example, Wirtzfeld *et al.*[35] have reported that interobserver and intraobserver variability of mouse tumor volume measurements followed those reported in clinical studies with coefficients of variation from 4% to 14%. Future work will consider interobserver and intraobserver variability in delineating tumor and regions of cell death that were not assessed in this study.

The transducer used in this work had a center frequency of 25 MHz allowing a good balance between resolution (axial $\approx 70$ $\mu$m and lateral $\approx 200$ $\mu$m), penetration depth beyond 10 mm, and a good detection of tumor boundaries and hyperechoic regions. The signal of the hyperechoic regions and the rest of the tumor were equally affected by attenuation (e.g., approximately 0.06 dB/mm/MHz for hyperechoic regions and the rest of the tumor).[14] For tumor sizes ($\leq 10$ mm in depth), the ultrasound beam penetrated the full extent of the tumor; hence, it was possible to detect the hyperechoic regions in the ultrasound images of these tumors. However, the ultrasound signal could be significantly attenuated in tumors larger than 10 mm in depth. In this case, transducers with a better penetration depth, e.g., using linear array technology, and algorithms to compensate for signal attenuation with depth can provide a good detection of hyperechoic regions.

The second category addresses issues associated with the reconstruction of the histological volume and registration of histological and ultrasound images. Anatomical landmarks (e.g., bundles of muscles, skin) which are visible on both histological and ultrasound images can assist with the histological volume reconstruction and registration. Identifying correct correspondence between anatomical landmarks in consecutive histological slides and corresponding ultrasound images is difficult because these may not be consistently visible across all histological sections and in both image sets. Fiducial markers created by inserted needles were used in this work to avoid misalignments that can compromise reconstruction of cell death volume that was very small in the PC3 tumor. The same technique could help with the histological volume reconstruction for C666–1 and FaDu tumors. However, it could also greatly damage the area of cell death. For this reason, the use of needles was restricted to the PC3 tumor. The validation of the histological volume reconstruction and registration with ultrasound images were challenging because the number of naturally occurring anatomical markers that can be visible on consecutive histological slides is limited. For instance, in order to assess the accuracy of reconstruction, markers independent of those used in the histological volume reconstruction have to be used. In this study, three naturally occurring markers (or markers created by the inserted needles) were used for histological reconstruction and registration with ultrasound images. If a fourth marker existed, it was used to assess the matching. Ongoing work in our laboratory seeks to develop techniques of injecting appropriate fiducial markers that can be visible on both data sets, histological and tissue images. These can assist with histological volume reconstruction, registration with imaging, as well as assessment of registration accuracy.[29]

The third category addresses factors linked to the definition of cell death in histology and its representation in ultrasound images. Since the segmentation of cell death was performed on high-resolution histological images, it was straightforward to identify the regions exhibiting nuclei condensation and fragmentation as typical characteristics of cell death. However, as indicated by previous works, ultrasound imaging can be sensitive to other types of cell structural damage[18,19,36] that do not fall under this definition. These could also result in differences in tissue acoustic properties and, consequently, changes of tissue echogeneity in ultra-

sound images. Different patterns of cell structural damage were often observed in the histology of the PC3 tumor [Fig. 4(C)], and may explain the difference of 44% observed between representation of cell death in ultrasound and histology in this tumor. A work in progress in our laboratory seeks to understand whether these histological features are consequences of damage to tumor microvasculature following radiotherapy[26] or tissue microedema (inflammation). Damage of tumor microvasculature can ultimately result in cell death in those regions. However, tissue microedema can interfere with the assessment of cell death causing false positive results. In this case, ultrasound tissue characterization methods using radiofrequency spectrum analysis[14,37–39] can be used, additionally to ultrasound imaging, to refine the detection of cell death.

High frequency ultrasound has the capability to assess cell death noninvasively. Therefore, it can aid in the development of novel targeted therapies in preclinical settings, can provide input to individualized adaptive treatment planning, and has a potential to improve clinical trial efficiency. Considering future clinical applications of the technique described in this work, head and neck tumors could be accessed in humans using endoscopic probes working at 10–20 MHz.[40]

This study described a method that compares the volume and localization of cell death, assessed from histology, to the volume and localization of cell death surrogate derived as hyperechoic regions from ultrasound imaging. This estimation can depend on tumor type, histological processing, ultrasound machine-scanning parameters, and, potentially, on the applied therapy. The method could be applied on a limited number of mice to provide a relationship between the true cell death (derived from histology) and surrogate cell death derived from ultrasound images. Then, these findings can provide input into longitudinal studies that use ultrasound imaging to assess cell death noninvasively.

Ultrasound imaging is a low cost portable technique. The key advantage of this technique is that the image contrast is caused by changes in the physical properties of dying cells. Therefore, the subject can be imaged before and multiple times during the treatment without the need of injecting specialized contrast agents as required by other techniques (e.g., PET and DCE-MRI). An early indicator of treatment response would be of great value to tailor treatments to individual patients and particularly promising in multistage interventions or combination treatments.

A penetration depth of 2–5 cm at the frequencies of 30 down to 10 MHz allows the technique to be applicable to a variety of tumor types such as skin cancers, certain cancers of the breast, and cancers that can be reached with endoscopic probes such as nasopharyngeal and gastrointestinal cancers. An ongoing work in detecting cell death at lower ultrasound frequency of 5–10 MHz (Ref. 41) may extend the range of applications to other tumor sites seated deeper into the body.

In conclusion, a method to evaluate the use of mid-frequency to high frequency ultrasound imaging technique to detect cell death following radiotherapy by comparing the geometry of cell death assessed from ultrasound with that assessed from histology was developed. The good agreement between cell death representation in histological and ultrasound images for head and neck cancer mouse models (C666–1 and FaDu) indicated that high frequency ultrasound is capable of detecting early response to radiotherapy in this type of tumors. The result obtained for PC3 tumor suggested that it is essential to perform a histological validation of ultrasound imaging for each specific treatment and tumor type. Other methods, additional to ultrasound imaging, i.e., ultrasound tissue characterization techniques, might be required to refine the detection of cell death in some tumors.

## ACKNOWLEDGMENTS

Dr. Kristy Brock and Dr. Gregory Czarnota are each supported through a Cancer Care Ontario Research Chair and Dr. Michael Kolios is supported through a Canada Research Chair. Part of the work was supported by American Institute of Ultrasound in Medicine's Endowment for Education and Research Grant and Canadian Institutes of Health Research Strategic Training Fellowship Excellence in Radiation Research for the 21st Century to Dr. Roxana Vlad. The authors thank Dr. Azza Al-Mahrouki and Anoja Giles for technical support, MORFEUS team for valuable discussion, and Dr. Fei-Fei Liu for providing some of the cell lines used in this work.

[a]Conflict of Interest Notification: There are no actual conflicts of interest.

[b]Author to whom correspondence should be addressed. Electronic mail: rvlad@lakeridgehealth.on.ca; Present address: Department of Radiation Oncology, R. S. McLaughlin Durham Regional Cancer Centre, Lakeridge Health, 1 Hospital Court, Oshawa, Ontario L1G 2B9, Canada; Telephone: 905-576-8711 x 5302.

[1]C. C. Jaffe, "Measures of response: RECIST, WHO, and new alternatives," J. Clin. Oncol. **24**, 3245–3251 (2006).

[2]E. A. Eisenhauer *et al.*, "New response evaluation criteria in solid tumours: Revised RECIST guideline (version 1.1)," Eur. J. Cancer **45**, 228–247 (2009).

[3]L. C. Michaelis and M. J. Ratain, "Measuring response in a post-RECIST world: From black and white to shades of grey," Nat. Rev. Cancer **6**, 409–414 (2006).

[4]K. Brindle, "New approaches for imaging tumour responses to treatment," Nat. Rev. Cancer **8**, 94–107 (2008).

[5]W. A. Weber, V. Petersen, B. Schmidt, L. Tyndale-Hines, T. Link, C. Peschel, and M. Schwaiger, "Positron emission tomography in non-small-cell lung cancer: Prediction of response to chemotherapy by quantitative assessment of glucose use," J. Clin. Oncol. **21**, 2651–2657 (2003).

[6]K. C. Lee, D. A. Bradley, M. Hussain, C. R. Meyer, T. L. Chenevert, J. A. Jacobson, T. D. Johnson, C. J. Galban, A. Rehemtulla, K. J. Pienta, and B. D. Ross, "A feasibility study evaluating the functional diffusion map as a predictive imaging biomarker for detection of treatment response in a patient with metastatic prostate cancer to the bone," Neoplasia **9**, 1003–1011 (2007).

[7]C. Tsien, D. Gomez-Hassan, T. L. Chenevert, J. Lee, T. Lawrence, R. K. Ten Haken, L. R. Junck, B. Ross, and Y. Cao, "Predicting outcome of patients with high-grade gliomas after radiotherapy using quantitative analysis of T1-weighted magnetic resonance imaging," Int. J. Radiat. Oncol., Biol., Phys. **67**, 1476–1483 (2007).

[8]W. A. Weber and H. Wieder, "Monitoring chemotherapy and radiotherapy of solid tumors," Eur. J. Nucl. Med. Mol. Imaging **33**, 27–37 (2006).

[9]P. J. Hoskin, M. I. Saunders, K. Goodchild, M. E. Powell, N. J. Taylor, and H. Baddeley, "Dynamic contrast enhanced magnetic resonance scanning as a predictor of response to accelerated radiotherapy for advanced head and neck cancer," Br. J. Radiol. **72**, 1093–1098 (1999).

[10]S. Kim, L. Loevner, H. Quon, E. Sherman, G. Weinstein, A. Kilger, and H. Poptani, "Diffusion-weighted magnetic resonance imaging for predict-

ing and detecting early response to chemoradiation therapy of squamous cell carcinomas of the head and neck," Clin. Cancer Res. **15**, 986–994 (2009).

[11]S. Kim, L. A. Loevner, H. Quon, A. Kilger, E. Sherman, G. Weinstein, A. Chalian, and H. Poptani, "Prediction of response to chemoradiation therapy in squamous cell carcinomas of the head and neck using dynamic contrast-enhanced MR imaging," AJNR Am. J. Neuroradiol. **31**, 262–268 (2010).

[12]J. A. Loncaster, B. M. Carrington, J. R. Sykes, A. P. Jones, S. M. Todd, R. Cooper, D. L. Buckley, S. E. Davidson, J. P. Logue, R. D. Hunter, and C. M. West, "Prediction of radiotherapy outcome using dynamic contrast enhanced MRI of carcinoma of the cervix," Int. J. Radiat. Oncol., Biol., Phys. **54**, 759–767 (2002).

[13]B. Bone, B. K. Szabo, L. G. Perbeck, B. Veress, and P. Aspelin, "Can contrast-enhanced MR imaging predict survival in breast cancer?," Acta Radiol. **44**, 373–378 (2003).

[14]R. M. Vlad, S. Brand, A. Giles, M. C. Kolios, and G. J. Czarnota, "Quantitative ultrasound characterization of responses to radiotherapy in cancer mouse models," Clin. Cancer Res. **15**, 2067–2075 (2009).

[15]B. Banihashemi, R. Vlad, B. Debeljevic, A. Giles, M. C. Kolios, and G. J. Czarnota, "Ultrasound imaging of apoptosis in tumor response: Novel preclinical monitoring of photodynamic therapy effects," Cancer Res. **68**, 8590–8596 (2008).

[16]G. J. Czarnota, M. C. Kolios, J. Abraham, M. Portnoy, F. P. Ottensmeyer, J. W. Hunt, and M. D. Sherar, "Ultrasound imaging of apoptosis: High-resolution non-invasive monitoring of programmed cell death in vitro, in situ and in vivo," Br. J. Cancer **81**, 520–527 (1999).

[17]L. R. Taggart, R. E. Baddour, A. Giles, G. J. Czarnota, and M. C. Kolios, "Ultrasonic characterization of whole cells and isolated nuclei," Ultrasound Med. Biol. **33**, 389–401 (2007).

[18]R. M. Vlad, N. M. Alajez, A. Giles, M. C. Kolios, and G. J. Czarnota, "Quantitative ultrasound characterization of cancer radiotherapy effects in vitro," Int. J. Radiat. Oncol., Biol., Phys. **72**, 1236–1243 (2008).

[19]R. M. Vlad, "Quantitative ultrasound characterization of responses to radiotherapy in vitro and in vivo," Ph.D. dissertation, University of Toronto, 2009.

[20]R. P. H. Ian, F. Tannock, R. G. Bristow, and L. Harrington, *The Basic Science of Oncology* (McGraw-Hill, New York, 2004).

[21]E. Namati, J. De Ryk, J. Thiesse, Z. Towfic, E. Hoffman, and G. McLennan, "Large image microscope array for the compilation of multimodality whole organ image databases," Anat. Rec. **290**, 1377–1387 (2007).

[22]G. M. Clarke, S. Eidt, L. Sun, G. Mawdsley, J. T. Zubovits, and M. J. Yaffe, "Whole-specimen histopathology: A method to produce whole-mount breast serial sections for 3-D digital histopathology imaging," Histopathology **50**, 232–242 (2007).

[23]R. S. Lazebnik, M. S. Breen, J. S. Lewin, and D. L. Wilson, "Automatic model-based evaluation of magnetic resonance-guided radio frequency ablation lesions with histological correlation," J. Magn. Reson Imaging **19**, 245–254 (2004).

[24]L. S. Taylor, B. C. Porter, G. Nadasdy, P. A. di Sant'Agnese, D. Pasternack, Z. Wu, R. B. Baggs, D. J. Rubens, and K. J. Parker, "Three-dimensional registration of prostate images from histology and ultrasound," Ultrasound Med. Biol. **30**, 161–168 (2004).

[25]G. J. Czarnota and M. C. Kolios, "Ultrasound detection of cell death," Imaging Medicine **2**, 17–28 (2010).

[26]G. J. Czarnota, R. Karshafian, A. Giles, B. Banihashemi, J. Lee, A. Cassie, and P. Burns, "Microbubble and ultrasound enhancement of radiation-induced tumour cell death in vivo," Abstract, AIUM Official Proceedings, 2009, p. S31.

[27]S. T. Cheung, D. P. Huang, A. B. Hui, K. W. Lo, C. W. Ko, Y. S. Tsang, N. Wong, B. M. Whitney, and J. C. Lee, "Nasopharyngeal carcinoma cell line (C666-1) consistently harbouring Epstein-Barr virus," Int. J. Cancer **83**, 121–126 (1999).

[28]J. H. Li, M. Chia, W. Shi, D. Ngo, C. A. Strathdee, D. Huang, H. Klamut, and F. F. Liu, "Tumor-targeted gene therapy for nasopharyngeal carcinoma," Cancer Res. **62**, 171–178 (2002).

[29]D. M. McGrath, R. M. Vlad, D. F. Warren, and K. K. Brock, "Fiducial markers for correlation of whole-specimen histopathology with MR imaging at 7 tesla," Med. Phys. **37**, 2321–2328 (2010).

[30]J. M. Balter, K. K. Brock, K. L. Lam, D. Tatro, L. A. Dawson, D. L. McShan, and R. K. Ten Haken, "Evaluating the influence of setup uncertainties on treatment planning for focal liver tumors," Int. J. Radiat. Oncol., Biol., Phys. **63**, 610–614 (2005).

[31]M. Garcia-Barros, F. Paris, C. Cordon-Cardo, D. Lyden, S. Rafii, A. Haimovitz-Friedman, Z. Fuks, and R. Kolesnick, "Tumor response to radiotherapy regulated by endothelial cell apoptosis," Science **300**, 1155–1159 (2003).

[32]D. H. Abramson, A. C. Schefler, D. Almeida, and R. Folberg, "Optic nerve tissue shrinkage during pathologic processing after enucleation for retinoblastoma," Arch. Ophthalmol. (Chicago) **121**, 73–75 (2003).

[33]H. Boonstra, J. W. Oosterhuis, A. M. Oosterhuis, and G. J. Fleuren, "Cervical tissue shrinkage by formaldehyde fixation, paraffin wax embedding, section cutting and mounting," Virchows Arch. A: Pathol. Anat. Histopathol. **402**, 195–201 (1983).

[34]B. Pritt, J. J. Tessitore, D. L. Weaver, and H. Blaszyk, "The effect of tissue fixation and processing on breast cancer size," Hum. Pathol. **36**, 756–760 (2005).

[35]L. A. Wirtzfeld, K. C. Graham, A. C. Groom, I. C. Macdonald, A. F. Chambers, A. Fenster, and J. C. Lacefield, "Volume measurement variability in three-dimensional high-frequency ultrasound images of murine liver metastases," Phys. Med. Biol. **51**, 2367–2381 (2006).

[36]R. M. Vlad, G. J. Czarnota, A. Giles, M. D. Sherar, J. W. Hunt, and M. C. Kolios, "High-frequency ultrasound for monitoring changes in liver tissue during preservation," Phys. Med. Biol. **50**, 197–213 (2005).

[37]B. L. McFarlin, W. D. O'Brien, Jr., M. L. Oelze, J. F. Zachary, and R. C. White-Traut, "Quantitative ultrasound assessment of the rat cervix," J. Ultrasound Med. **25**, 1031–1040 (2006).

[38]M. L. Oelze, W. D. O'Brien, Jr., J. P. Blue, and J. F. Zachary, "Differentiation and characterization of rat mammary fibroadenomas and 4T1 mouse carcinomas using quantitative ultrasound imaging," IEEE Trans. Med. Imaging **23**, 764–771 (2004).

[39]M. L. Oelze and J. F. Zachary, "Examination of cancer in mouse models using high-frequency quantitative ultrasound," Ultrasound Med. Biol. **32**, 1639–1648 (2006).

[40]C. J. Lightdale and K. G. Kulkarni, "Role of endoscopic ultrasonography in the staging and follow-up of esophageal cancer," J. Clin. Oncol. **23**, 4483–4489 (2005).

[41]G. J. Czarnota, N. Papanicolau, J. Lee, R. Karshafian, A. Giles, and M. C. Kolios, "Novel low-frequency ultrasound detection of apoptosis in vitro and in vivo [abstract]," Ultrason. Imaging **29**, 237–238 (2008).